An improved ptychographical phase retrieval algorithm for diffractive imaging

Andrew M. Maiden *, John M. Rodenburg

Department of Electrical and Electronic Engineering, University of Sheffield, S1 3JD, UK

ARTICLE INFO

ABSTRACT

The ptychographical iterative engine (or PIE) is a recently developed phase retrieval algorithm that employs a series of diffraction patterns recorded as a known illumination function is translated to a set of overlapping positions relative to a target sample. The technique has been demonstrated successfully at optical and X-ray wavelengths and has been shown to be robust to detector noise and to converge considerably faster than support-based phase retrieval methods. In this paper, the PIE is extended so that the requirement for an accurate model of the illumination function is removed.

© 2009 Elsevier B.V. All rights reserved.

1. Introduction

Iterative phase retrieval is one method of recovering a complex-valued reconstruction of a sample from measurement of its diffraction pattern. This is achieved by iteratively enforcing a set of constraints corresponding to the measurements taken and *a priori* knowledge of the system. In most practical manifestations of the technique, the measured diffraction pattern is the squared modulus of the Fourier transform of the object and this condition forms the first constraint set. An additional support constraint requires the reconstructed image to be zero-valued outside of a given region, corresponding to a finite support bounding the specimen in the physical experiment [1]. This support-based method has been successfully demonstrated at X-ray wavelengths [2,3] using a variable support as described in [4]. Further examples of common constraints are nonnegativity, atomicity and realness [5]. Low-resolution images of a sample have also been used as a constraint in electron microscopy [6].

Recently a number of algorithms have sought to recover phase using sets of diffraction patterns, with diversity between the patterns introduced by varying the experimental conditions. This approach has the advantage of removing the need for a finite object support (which can prove difficult to engineer) and algorithms using these data exhibit improved robustness and convergence speed over methods that use a single diffraction pattern. For examples, see [7–9]. The ptychographical iterative engine (PIE) [10] introduces diffraction pattern diversity by

scanning a localised illuminating 'probe' wavefront across a transmissive sample, recording diffraction patterns at a set of overlapping probe positions—an approach that has been shown to work well at optical [11] and X-ray wavelengths [12]. A drawback of the PIE is the need to accurately model the localised wavefront illuminating the target object. At best this can be very time-consuming, whilst at worst accurate knowledge of the phase of the illuminating beam may be impossible to measure with great enough accuracy. In a recently published paper [13] this problem was addressed using a projection-between-sets algorithm capable of solving for both the sample and the illuminating wavefront, whilst a non-linear optimisation approach was employed in [14] to solve for the probe as well as for errors in the probe positions. Here we present an alternative algorithm, a direct extension of the original PIE, that demonstrates improved convergence speed and robustness to noise.

2. Two ptychographical algorithms

A ptychographic data set is obtained by collecting a series of J far-field diffraction patterns generated by the interaction of a transmissive sample with a localised probe wavefront. The probe may be formed by an aperture close to the plane of the sample, or by the focussing of a beam using a lens. Alternatively, planar illumination can be used and an aperture placed beyond the sample, in which case the resulting reconstruction focusses at the plane of the aperture and must be back-propagated to recover an in-focus object estimate. Between each diffraction pattern measurement, the probe and sample are moved relative to one another such that a different region of the sample is illuminated

strongly in each position. Measurements continue until the area of interest of the sample has been covered by a series of overlapping probe positions, with good results requiring an overlap of around 60–70%.

It is assumed that the interaction between the sample and the probe can be modelled by a complex multiplication; the validity of this assumption is investigated further in [13]. The wavefront exiting the sample is termed the exit-wave and it is further assumed that its propagation to the plane of the detector can be modelled by a Fourier transform, implying that a high degree of coherence is required from the probe at the plane of the sample. Subsequently, the intensity of the wavefront incident at the detector is

$$I_j(\mathbf{u}) = |\mathscr{F}[O(\mathbf{r})P(\mathbf{r} - \mathbf{R}_j)]|^2, \qquad (1)$$

where $\mathbf{r}$ and $\mathbf{u}$ are suitable real-space and reciprocal-space coordinate vectors and the probe and object wavefronts are denoted by $P(\mathbf{r})$ and $O(\mathbf{r})$, respectively. The vector $\mathbf{R}_j$ encodes the relative shift introduced between the object and probe before recording the intensity of the jth diffraction pattern.

The task of a ptychographical algorithm is to associate the correct phases with each diffraction pattern and so via an inverse Fourier transform recover the amplitude and phase of each exit-wave. The probe and object wavefronts can then be calculated as two functions that satisfy

$$O(\mathbf{r})P(\mathbf{r} - \mathbf{R}_j) = \chi_j(\mathbf{r}) \quad \forall j, \qquad (2)$$

where the jth exit-wave is termed $\chi_j(\mathbf{r})$. These solutions are not necessarily unique, for example $[cO(\mathbf{r}), c^{-1}P(\mathbf{r} - \mathbf{R}_j)]$, where c is a scalar constant, is also a solution whilst the invariance of the Fourier transform to lateral shifts means that $[O(\mathbf{r} - \mathbf{a}),$ $P(\mathbf{r} - \mathbf{R}_j - \mathbf{a})]$, where $\mathbf{a}$ is a constant offset vector, will also satisfy Eq. (1).

2.1. The parallel projections algorithm

The algorithm introduced by [13] and further detailed in [15] frames the problem of recovering the exit-wave phases, and hence estimates of the probe and object waveforms, as a search for the intersection of two sets in a complex space of dimensions $M \times N \times J$, where each of the J recorded diffraction patterns contain $M \times N$ pixels. The first constraint set encloses valid solutions to Eq. (2), that is those exit-waves that can be factored into two functions with the appropriate relative shifts. The second contains solutions to Eq. (1), the exit-waves whose Fourier transform amplitudes match the square-root of the recorded intensities. Once the constraint sets have been defined, various strategies based on alternating projections can be used to find their intersection [16]—in [13,15] the 'difference map' method is used, which is similar to a relaxed version of Fienup's hybrid input–output method. This formulation is close to the extended projections onto convex sets (ePOCS) method described in [17,18] where J sets are defined in an $M \times N$ dimensional space and projections carried out in parallel onto these sets. Because of this parallelism, we term this method the parallel PIE, or pPIE.

2.2. The extended ptychographical engine

Here we introduce the extended PIE, or 'ePIE', whose operation is illustrated in Fig. 1. Initial guesses, labelled $O_0(\mathbf{r})$ and $P_0(\mathbf{r})$, of the object and probe waveforms are required to begin the algorithm. Generally the initial object guess is taken as free-space and the initial probe waveform is taken as a support function roughly the size of the intense region of the probe wavefront. Each diffraction pattern is considered in turn, with both the object and probe
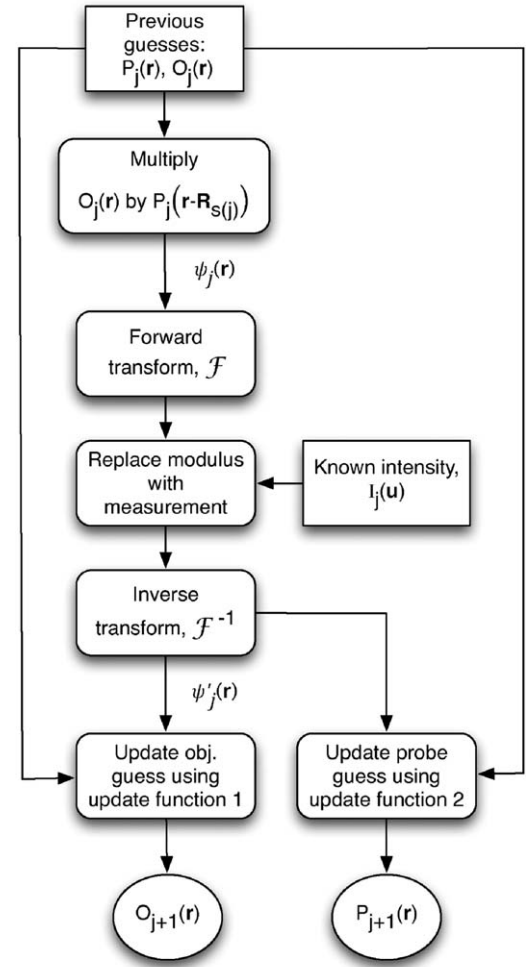
Fig. 1. Flowchart of the ePIE method. At $j = 0$, initial guesses at both the sample and probe waveforms are provided to the algorithm; a free-space guess at the sample and a support of roughly the correct size for the probe.

guesses being updated at each step—an approach that leads to a much quicker rate of convergence. In this sense the ePIE can be thought of as a serial equivalent to the pPIE and considered in the framework set out in [17,18].

The diffraction patterns are addressed in a random sequence $s(j)$. Beginning with pattern $s(0)$, a guess at the exit-wave χ_j is formed by multiplying the current object guess by the appropriately shifted probe guess, giving

$$\psi_j(\mathbf{r}) = O_j(\mathbf{r})P_j(\mathbf{r} - \mathbf{R}_{s(j)}). \qquad (3)$$

The presence of zeros in the exit-wave can result in stagnation of phase retrieval algorithms [19]; it is not clear to what extent ptychography suffers from this problem and the effect is not investigated further here. In a manner common to most phase retrieval techniques, the modulus of the Fourier transform of this exit-wave is next replaced with the (positive) square-root of the $s(j)$th diffraction pattern recording so that

$$\Psi_j(\mathbf{u}) = \sqrt{I_{s(j)}(\mathbf{u})} \frac{\mathscr{F}[\psi_j(\mathbf{r})]}{|\mathscr{F}[\psi_j(\mathbf{r})]|}. \qquad (4)$$

An updated exit-wave is then calculated via an inverse Fourier transform,

$$\psi'_j(\mathbf{r}) = \mathscr{F}^{-1}[\Psi_j(\mathbf{u})], \qquad (5)$$

and updated object and probe guesses are extracted from this result using two update functions. Update function 1 updates the current object guess and is given by

$$O_{j+1}(\mathbf{r}) = O_j(\mathbf{r}) + \alpha \frac{P_j^*(\mathbf{r} - \mathbf{R}_{s(j)})}{|P_j(\mathbf{r} - \mathbf{R}_{s(j)})|_{\max}^2}(\psi_j^{'}(\mathbf{r}) - \psi_j(\mathbf{r})). \qquad (6)$$

This step mirrors the update function described in the original PIE. A new object guess is formed by dividing out the current probe from the corrected exit-wave and taking a weighted average of this function and the current object guess, with weights proportional to the intensity of the current probe function estimate. The constant α can be adjusted to alter the step-size of the update, although $\alpha = 1$ has been used for the results in this paper.

The update of the probe proceeds in a similar fashion, with update function 2 being given by

$$P_{j+1}(\mathbf{r}) = P_j(\mathbf{r}) + \beta \frac{O_j^*(\mathbf{r} + \mathbf{R}_{s(j)})}{|O_j(\mathbf{r} + \mathbf{R}_{s(j)})|_{\max}^2}(\psi_j^{'}(\mathbf{r}) - \psi_j(\mathbf{r})). \qquad (7)$$

Here the roles of the object and probe have been reversed, but the principles remain the same. β can be adjusted to alter the step-size of the update similarly to α in update function 1, again $\beta = 1$ has been used for the results presented here.

The process continues with diffraction pattern $s(1), s(2), \ldots, s(J)$ until each of the J diffraction patterns have been used to update the object and probe guesses, at which point a single ePIE iteration has been completed.

3. Simulation results

The ePIE has been compared to the parallel projection method and to the original PIE method using simulated diffraction patterns. Two images, each of 256×256 pixels were used as the object phase and modulus profiles. The modulus image was scaled to values in the range 0.2–1 and the phase to values between $\pm\pi$. Fig. 2 shows the area of the simulated object modulus covered by 144 different probe positions, which are assumed known by the two algorithms. A random offset was added to a regular 12×12 grid to generate these positions, since (as explained in [15]) a periodic grid can lead to a periodic pattern appearing in the reconstruction. The probe was generated by propagating an aperture a short distance and is shown in the insets of Fig. 2. Specks of simulated dust were added to the aperture, something that has often been noticed in practical experiments.

Far-field diffraction patterns were simulated from this arrangement and Poisson distributed noise introduced such that the approximate total count of each pattern was 10^5. As an initial guess at the probe a circular support function was used whose
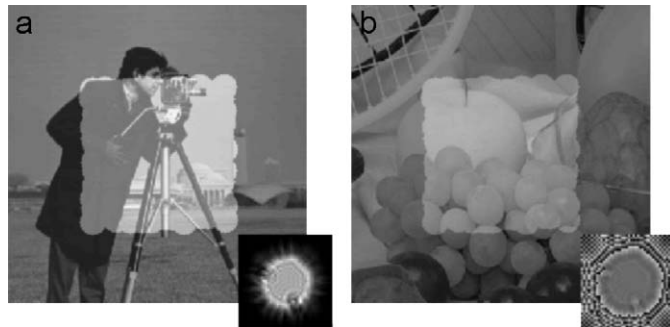
diameter was approximately 2 pixels too wide, simulating an inaccurate knowledge of the aperture size in a real experiment. In line with the literature this probe estimate was not updated until 20 iterations of the pPIE had been completed. The ePIE does not require this initial step, although in the results here a single iteration without the probe update was included. Free-space was used as an initial guess at the object.

Since the true object wavefront, denoted $O(\mathbf{r})$, is known in the simulated case, the convergence of each algorithm can be measured directly using the normalised RMS error metric
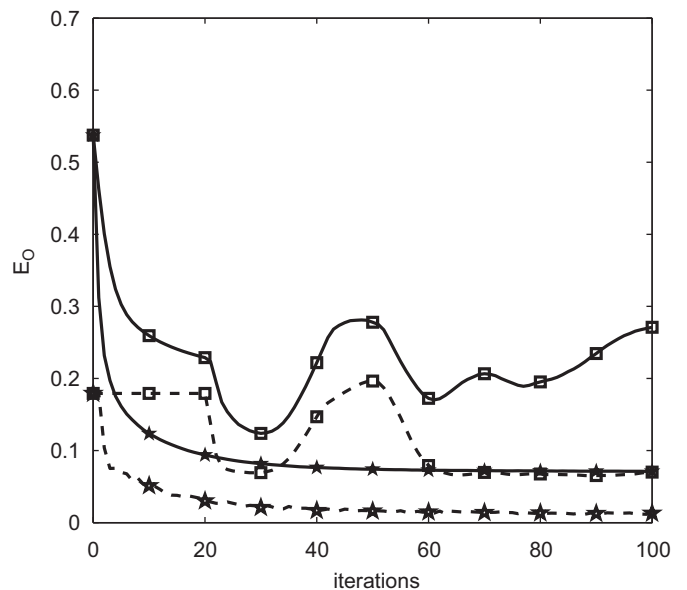
$$E_O(n) = \frac{\sum_{\mathbf{r}}|O(\mathbf{r}) - \gamma O_n(\mathbf{r})|^2}{\sum_{\mathbf{r}}|O(\mathbf{r})|^2}. \qquad (8)$$

The parameter γ allows for the multiplication of the object by a constant and for a constant phase offset, with

$$\gamma = \frac{\sum_{\mathbf{r}}O(\mathbf{r})O_n^*(\mathbf{r})}{\sum_{\mathbf{r}}|O_n(\mathbf{r})|^2}. \qquad (9)$$

$O_n(\mathbf{r})$ is the reconstructed object distribution after n iterations of the parallel projection algorithm, or the result of the ePIE after each diffraction pattern has been used to update the reconstruction n times. $E_O(n)$ was calculated over the 100×100 pixel area at the centre of the reconstruction that was well covered by a number of overlapping probe positions. A sub-pixel registration algorithm was used to account for lateral translations of the reconstruction with respect to the original object [20].

Fig. 3 plots the evolution of E_O over 100 iterations of the two algorithms. At this level of noise and with an inaccurate initial guess at the probe, the pPIE does not converge well. For the first 20 iterations during which the probe is not updated the object reconstruction shows only minor improvement due to the inaccurate initial probe guess. As the algorithm progresses the updated probe tends to drift and the object smears as a result, leading to the erratic shape of the error plot. In contrast, the ePIE behaves well in spite of a high level of noise and the inaccurate probe model. Its convergence is significantly quicker in terms of iterations, and each iteration takes between a half and a third of the time. The amplitude parts of the final reconstructions are


Fig. 2. An illustration of the object, probe and probe positions used to generate the simulated diffraction patterns. The highlighted area corresponds to the area of the sample strongly illuminated in at least one probe position. The insets illustrate the probe function used. (a) Simulated object and probe amplitudes. (b) Simulated object and probe phases.

Fig. 3. Convergence of the pPIE and ePIE. Simulated diffraction data were used with Poisson distributed noise and an approximate count of 10^5. The square markers indicate results from the pPIE and star markers correspond to the ePIE. Dashed traces show the progress of the probe reconstruction and solid traces the error in the central 100×100 pixels of the object.
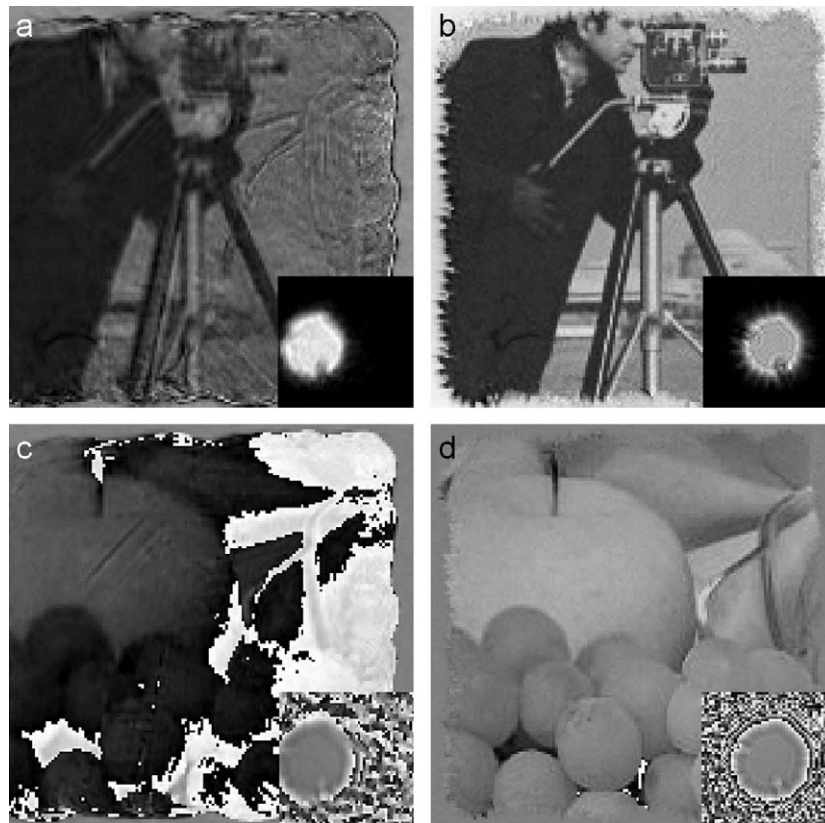
Fig. 4. Reconstructions from the two algorithms using noisy simulated data. The probe in the pPIE reconstruction has drifted to the right, causing a degree of blurring in the object reconstruction. (a) pPIE-reconstructed object (main figure) and probe (inset) amplitudes. (b) ePIE-reconstructed object (main figure) and probe (inset) amplitudes. (c) pPIE-reconstructed object (main figure) and probe (inset) phases. (d) ePIE-reconstructed object (main figure) and probe (inset) phases.
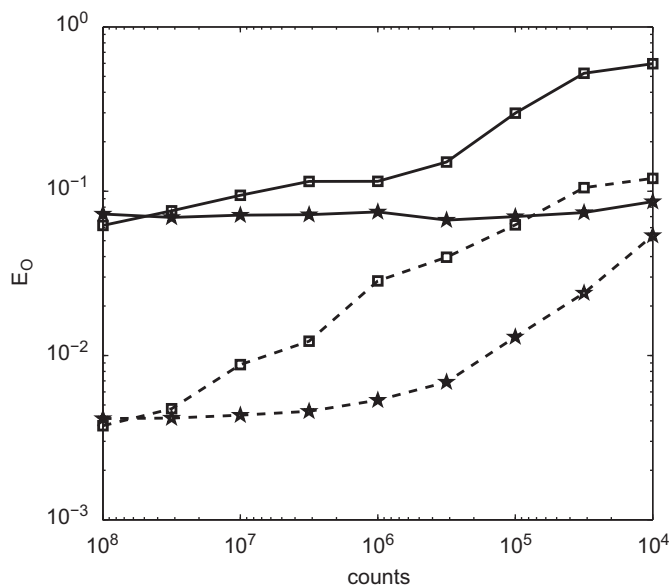
Fig. 5. The robustness to noise of the pPIE and ePIE. Poisson distributed shot noise was added to simulated diffraction patterns giving approximate counts per diffraction pattern as indicated. One hundred iterations of each algorithm were performed. Square markers are assigned to the pPIE and star markers to the ePIE. Dashed traces show the error in the probe reconstruction, solid traces show the error in the central 100×100 pixels of the object.
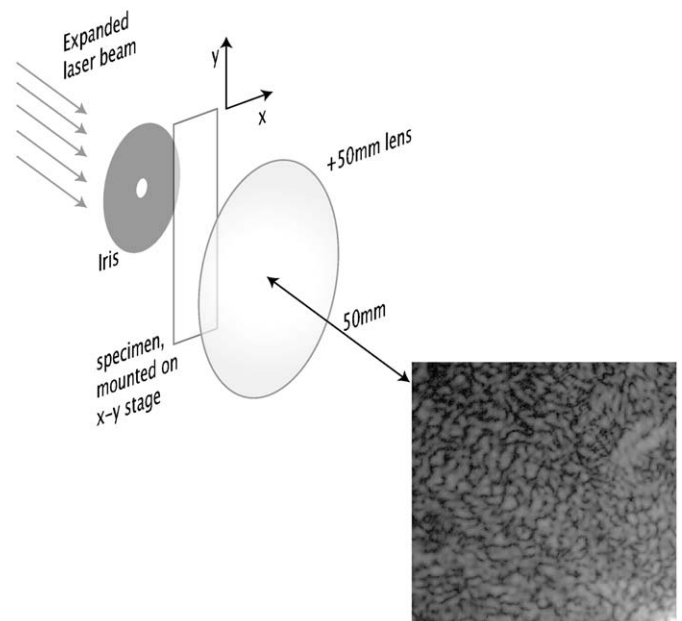
Fig. 6. The optical setup used to capture a ptychographical data set. The top lefthand quarter of one of the recorded diffraction patterns is illustrated, showing significant amounts of noise (logarithmic scale).

shown in Fig. 4. The pPIE reconstruction is severely degraded by artifacts and blurring, in part caused by the drifting of the probe shown in the inset of the figure. The algorithm has succeeded in recovering the asymmetry of the probe and some of its fringe structure, but there is a significant degree of 'cross-talk' between the phase and amplitude parts of the object reconstruction. The ePIE has performed significantly better. Although the sharp edges of the original pattern and the fine fringes of the probe are lost, the low spatial frequency information is well reconstructed and there are no artifacts visible.

The simulation detailed above was repeated with an increasing level of noise introduced to the diffraction patterns. Fig. 5 plots the

Fig. 7. The progress of the error metric E_Ψ over 300 iterations of the PIE (triangles), pPIE (squares) and ePIE (stars). A simulated aperture of approximately the correct size was used as the initial probe guess. The PIE used this guess throughout the reconstruction, whilst the pPIE did not update the probe during the first 25 iterations. Both the pPIE and the ePIE were followed by 50 iterations of an error reduction algorithm after the 300 iterations had been completed.

final error value after 100 iterations of the p- and ePIE as the approximate count of each diffraction pattern decreases. At zero noise, the pPIE converges as quickly as the ePIE and to a similar error level. Both algorithms continue to perform well for high particle counts where the degree of noise is very low. At lower counts, the pPIE reconstruction begins to degrade whilst the ePIE performs remarkably well even when the noise is extremely high and a large part of each diffraction pattern records zero counts.
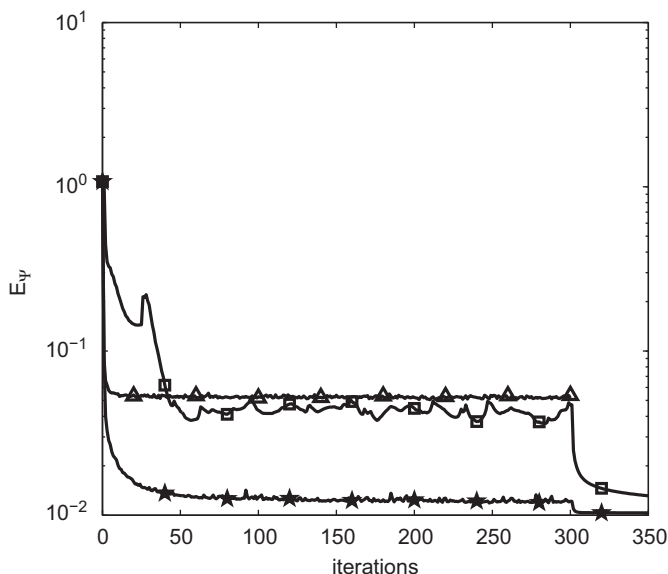
4. Optical bench results

An experiment has been conducted at optical wavelengths to assess the performance of the ePIE using real data and compare this to the pPIE. A ptychographical data set was collected using an iris aperture set at $\approx 700\,\mu m$ diameter to form a localised probe function, incident upon a conventional microscope slide containing a section from a bee's hind leg. The slide was placed approximately 2 mm downstream of the iris and attached to a motorised x–y stage. This was then translated to 100 positions in a 10×10 grid with a $210\,\mu m$ spacing, corresponding to $\approx 70\%$ probe overlap. A 50 mm convex lens was placed just behind the slide to form a far-field diffraction pattern on a CCD array placed in its back focal plane—the setup is illustrated in Fig. 6. Five frames at increasing exposure times were recorded from the CCD for each slide position and the results scaled and combined to increase the dynamic range of the detector to ≈ 18 bits. As Fig. 6 shows, a considerable amount of read-out and random noise was apparent in the diffraction patterns, especially in regions of low intensity corresponding to the longer camera exposure times.
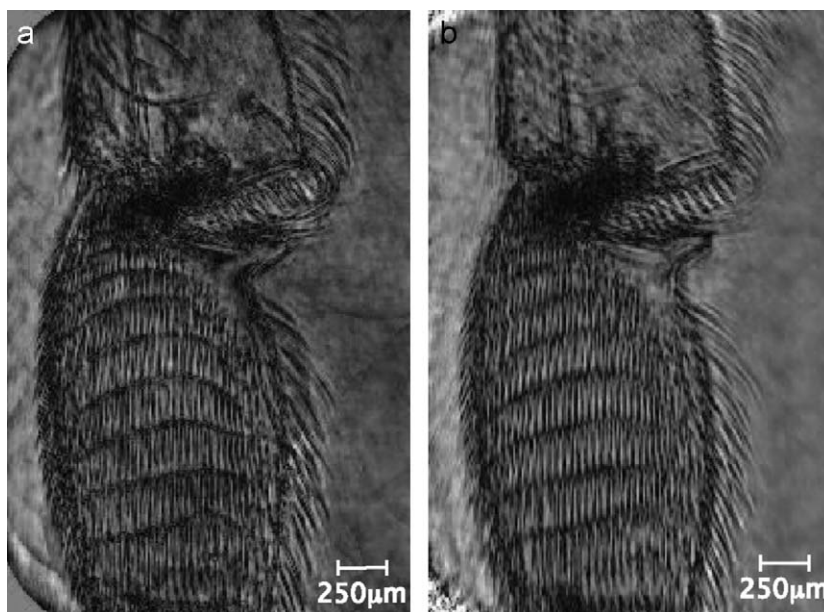
Since the true object wavefront is no longer available, Eq. (8) can no longer be used as an error measure. Instead, the normalised error in the diffraction patterns was measured after each full iteration of the algorithms as

$$E_\Psi = \frac{\sum_j \sum_{\mathbf{u}} |\sqrt{I_j(\mathbf{u})} - |\Psi_j(\mathbf{u})\|^2}{\sum_j \sum_{\mathbf{u}} I_j(\mathbf{u})}. \qquad (10)$$
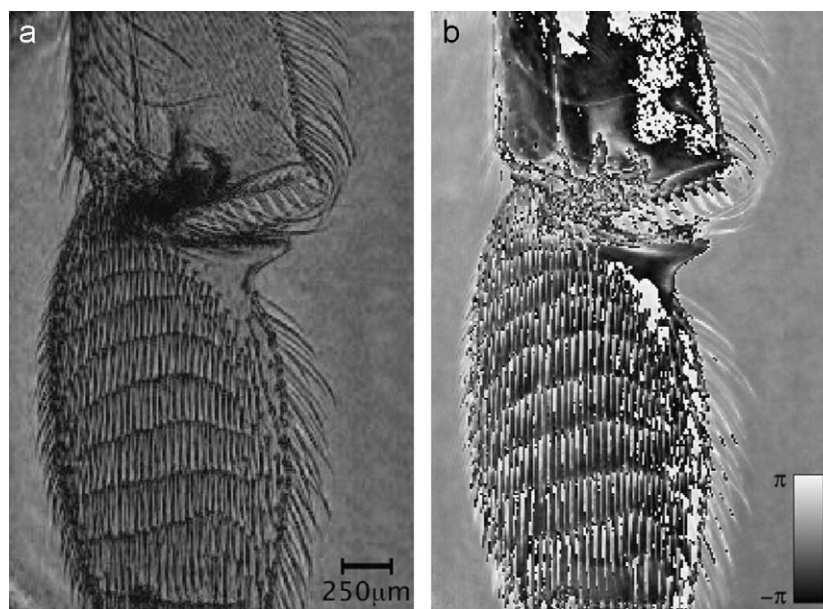
Each probe retrieval algorithm was cycled through 300 iterations with a support of roughly the right size and free-space being used


Fig. 8. The amplitudes of the final reconstructions resulting from the PIE and pPIE. (a) Amplitude of the PIE reconstruction. (b) Amplitude of the pPIE reconstruction.

Fig. 9. The amplitude and phase of the final reconstruction resulting from the ePIE. (a) Amplitude of the ePIE reconstruction. (b) Phase of the ePIE reconstruction.

as initial probe and object guesses, respectively. The initial probe guess was also used in an implementation of the original PIE for comparison. Fig. 7 plots the error metric of Eq. (10) as the reconstructions progress. As expected the PIE performs poorly given the poor probe model with which it was supplied. In the final reconstruction shown in Fig. 8(a) probe artifacts are visible and the bee's leg is blurred as the probe is not propagated to the plane of the sample. The behaviour of the pPIE is in line with that expected from this type of algorithm, as detailed in [1]. Generally, these algorithms are followed by a few iterations of an error reduction (ER) algorithm involving projections between the two constraint sets without any relaxation or reflection of the projections [21]. Carrying out this procedure for 50 iterations on the reconstruction from the pPIE significantly reduced the measured error as shown in the figure, but had little impact on the clarity of the reconstruction. The final reconstruction after 300 iterations of the pPIE and 50 iterations of an ER algorithm is shown in Fig. 8(b). The improvement over the PIE is apparent and there are no probe artifacts visible, but the image still appears blurred. The probe reconstruction shown in Fig. 10 shows clear Fresnel fringing demonstrating the attempt by the pPIE to find the focal plane of the sample, and an asymmetry corresponding to the eight leaves of the iris can also be seen. However, a vague regular structure has impressed itself upon the probe, perhaps due to the regular grid of probe positions used.

The ePIE was also supplemented by 50 iterations of an ER algorithm, the effect of which was a small improvement in the error measure as plotted in Fig. 7. It is also clear from the figure that after 100 iterations of the ePIE the reconstruction could be considered to have converged, the random fluctuations in the error being attributable to the random order in which the diffraction patterns are addressed at each iteration. Although the final error value is similar to that of the pPIE, the improvement in the clarity of the reconstruction is evident from Fig. 9. Detail within the bee's leg not apparent in the other reconstructions is clearly visible here and no probe artifacts can be seen. From Fig. 10, the probe itself contains several sets of fringes lost to the pPIE reconstruction and the leaves of the iris and a speck of dust are well resolved upon propagating the probe back to the plane of the aperture.
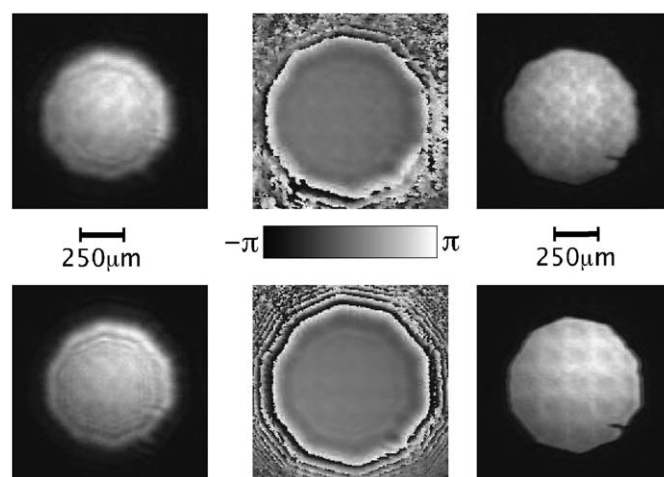
Fig. 10. Top line from left: pPIE probe amplitude, phase and probe at the plane of the iris. Bottom line from left: ePIE probe amplitude, phase and probe at the plane of the iris. Note the much better resolved fringes in the ePIE probe reconstruction and the resulting improvement in the image of the iris generated by back-propagating the probe wavefront. Both algorithms retain periodic artifacts from the regular grid of the probe positions; this can be circumvented by adding random offsets to each probe position.

5. Conclusions

The ePIE is a natural extension to the original PIE that enables both the object and probe wavefront to be recovered simultaneously. Consequently it delivers much improved reconstructions when an accurate probe model is difficult or impossible to derive, such as in X-ray and electron beam experiments. In this paper the original and ePIE methods have been compared with the algorithm described in [13], referred to here as the pPIE. The pPIE works extremely well if the diffraction patterns are low in noise and a reasonable guess at the probe function can be derived. However, it has been found that whilst both probe retrieval algorithms improve on the reconstruction resulting from the PIE, the ePIE provides speedier convergence and a greater robustness to noise. We have found that feeding the results from the ePIE into

an ER algorithm for a few iterations results in the best reconstructions. A third method of retrieving the probe [14] has not been investigated here, although the update of the probe and object at each step in the ePIE should allow it to retain its advantage in terms of convergence rate.

The ability to solve for the probe opens up a range of options to tailor the sample illumination to suit experimental conditions, for example working in the near-field or using a phase plate rather than an aperture. A number of interesting possibilities are currently being investigated at optical and X-ray wavelengths and using a transmission electron microscope.

Acknowledgements

References

[1] J.R. Fienup, Phase retrieval algorithms: a comparison, Appl. Opt. 21 (15) (1982) 2758–2769.
[2] B. Abbey, K.A. Nugent, G.J. Williams, J.N. Clark, A.G. Peele, M.A. Pfeifer, M.D. de Jonge, I. McNulty, Keyhole coherent diffractive imaging, Nat. Phys. 4 (2008) 394–398.
[3] H.N. Chapman, A. Barty, S. Marchesini, A. Noy, S.P. Hau-Riege, C. Cui, M.R. Howells, R. Rosen, H. He, J.C.H. Spence, U. Weierstall, T. Beetz, C. Jacobsen, D. Shapiro, High-resolution ab initio three-dimensional X-ray diffraction microscopy, J. Opt. Soc. Am. A 23 (2006) 1179–1200.
[4] S. Marchesini, H.N. Chapman, S.P. Hau-Riege, A. Noy, M.R. Howells, U. Weierstall, J.C.H. Spence, X-ray image reconstruction from a diffraction pattern alone, Phys. Rev. B 68 (2003) 140101(R).
[5] V. Elser, Phase retrieval by iterated projections, J. Opt. Soc. Am. A 20 (1) (2003) 40–55.
[6] W.J. Huang, J.M. Zuo, B. Jiang, K.W. Kwon, M. Shim, Sub-angström-resolution diffractive imaging of single nano-crystals, Nat. Phys. 5 (2009) 129–133.
[7] R.A. Gonsalves, Phase retrieval and diversity in adaptive optics, Opt. Eng. 21 (1982) 829–832.
[8] P. Bao, F. Zhang, G. Pedrini, W. Osten, Phase retrieval using multiple illumination wavelengths, Opt. Lett. 33 (4) (2008) 309–311.
[9] F. Zhang, G. Pedrini, W. Osten, Phase retrieval of arbitrary complex-valued fields through aperture-plane modulation, Phys. Rev. A 75 (2007) 043805.
[10] J.M. Rodenburg, H.M.L. Faulkner, A phase retrieval algorithm for shifting illumination, Appl. Phys. Lett. 85 (20) (2004) 4795–4797.
[11] J.M. Rodenburg, A.C. Hurst, A.G. Cullis, Transmission microscopy without lenses for objects of unlimited size, Ultramicroscopy 107 (2007) 227–231.
[12] J.M. Rodenburg, A.C. Hurst, A.G. Cullis, B.R. Dobson, F. Pfeiffer, O. Bunk, C. David, K. Jefimovs, I. Johnson, Hard-X-ray lensless imaging of extended objects, Phys. Rev. Lett. 98 (2007) 034801.
[13] P. Thibault, M. Dierolf, A. Menzel, O. Bunk, C. David, F. Pfeiffer, High-resolution scanning X-ray diffraction microscopy, Science 321 (2008) 379–382.
[14] M. Guizar-Sicairos, J.R. Fienup, Phase retrieval with transverse translation diversity: a nonlinear optimization approach, Opt. Express 16 (10) (2008) 7264–7278.
[15] P. Thibault, M. Dierolf, O. Bunk, A. Menzel, F. Pfeiffer, Probe retrieval in ptychographic coherent diffractive imaging, Ultramicroscopy 109 (2009) 338–343.
[16] S. Marchesini, A unified evaluation of iterative projection algorithms for phase retrieval, Rev. Sci. Instrum. 78 (2006).
[17] T. Kotzer, N. Cohen, J. Shamir, Generalized approach to projections onto convex constraint sets, in: Proceedings of the IAPR, vol. 12, 1994, vol. 3, 1994, pp. 77–81.
[18] Y. Censor, N. Cohen, T. Kotzer, J. Shamir, Summed squared distance error reduction by simultaneous multiprojections and applications, Appl. Math. Comput. 126 (2002) 157–179.
[19] J.R. Fienup, C.C. Wackerman, Phase-retrieval stagnation problems and solutions, J. Opt. Soc. Am. A 3 (11) (1986) 1897–1907.
[20] M. Guizar-Sicairos, S.T. Thurman, J.R. Fienup, Efficient subpixel image registration algorithms, Opt. Lett. 33 (2) (2008) 156–158.
[21] L.M. Bregman, The method of successive projection for finding a common point of convex sets, Sov. Math. Doklady 6 (1965) 688–692.